

# Towards automatic calibration of Fourier-Domain OCT for robot-assisted vitreoretinal surgery

Xuan Liu,<sup>1,\*</sup> Marcin Balicki,<sup>2</sup> Russell H. Taylor,<sup>2</sup> and Jin U. Kang<sup>1</sup>

<sup>1</sup>*Department of Electrical and Computer Engineering, Johns Hopkins University,  
3400 N. Charles St, Baltimore, Maryland 21211, USA*

<sup>2</sup>*Department of Computer Science, Johns Hopkins University,  
3400 N. Charles St, Baltimore, Maryland 21211, USA*

\*[xliu35@jhu.edu](mailto:xliu35@jhu.edu)

**Abstract:** We present a new real-time automatic spectral calibration (ASC) method for Fourier domain optical coherence tomography (FD OCT) that can be automatically performed by the system. The ASC method proposed can be performed during OCT scanning operation and does not require an external calibrating light source or a commercial optical spectrum analyzer. Spectral data used for calibration can be interferograms obtained from an arbitrary sample which may have complicated internal structures, such as ones found in biological tissue. Moreover, our ASC method incorporates known robot motion to calibrate physical pixel spacing of the A-scan in static or dynamic environments. Experimental results show that our ASC method can provide high-performance calibration for FD OCT in terms of axial resolution and ranging accuracy without increasing hardware complexity.

©2010 Optical Society of America

**OCIS codes:** (170.4500) Optical coherence tomography; (170.3880) Medical and biological imaging.

---

## References and links

1. S. Han, M. V. Sarunic, J. Wu, M. Humayun, and C. Yang, "Handheld forward-imaging needle endoscope for ophthalmic optical coherence tomography inspection," *J. Biomed. Opt.* **13**(2), 020505 (2008).
2. M. Balicki, J. Han, I. Iordachita, P. Gehlbach, J. Handa, J. U. Kang, and R. Taylor, "Single Fiber Optical Coherence Tomography Microsurgical Instruments for Computer and Robot-Assisted Retinal Surgery," *Proceedings of the MICCAI Conference, London*, pp. 108–115 (2009).
3. K. Zhang, W. Wang, J. Han, and J. U. Kang, "A surface topology and motion compensation system for microsurgery guidance and intervention based on common-path optical coherence tomography," *IEEE Trans. Biomed. Eng.* **56**(9), 2318–2321 (2009).
4. J. Han, M. Balicki, K. Zhang, X. Liu, J. Handa, R. Taylor, and J. U. Kang, "Common-path Fourier-domain Optical Coherence Tomography with a Fiber Optic Probe Integrated Into a Surgical Needle," *Proceedings of CLEO Conference* (2009).
5. Y. K. Tao, J. P. Ehlers, C. A. Toth, and J. A. Izatt, "Intraoperative spectral domain optical coherence tomography for vitreoretinal surgery," *Opt. Lett.* **35**(20), 3315–3317 (2010).
6. J. F. de Boer, B. Cense, B. H. Park, M. C. Pierce, G. J. Tearney, and B. E. Bouma, "Improved signal-to-noise ratio in spectral-domain compared with time-domain optical coherence tomography," *Opt. Lett.* **28**(21), 2067–2069 (2003).
7. R. Leitgeb, C. Hitzenberger, and A. Fercher, "Performance of fourier domain vs. time domain optical coherence tomography," *Opt. Express* **11**(8), 889–894 (2003), <http://www.opticsinfobase.org/oe/abstract.cfm?URI=oe-11-8-889>.
8. M. Choma, M. Sarunic, C. Yang, and J. Izatt, "Sensitivity advantage of swept source and Fourier domain optical coherence tomography," *Opt. Express* **11**(18), 2183–2189 (2003), <http://www.opticsinfobase.org/abstract.cfm?URI=oe-11-18-2183>.
9. X. Li, J. H. Han, X. Liu, and J. U. Kang, "Signal-to-noise ratio analysis of all-fiber common-path optical coherence tomography," *Appl. Opt.* **47**(27), 4833–4840 (2008).
10. U. Sharma, N. M. Fried, and J. U. Kang, "All-fiber Fizeau optical coherence tomography: sensitivity optimization and system analysis," *IEEE J. Quantum Electron.* **11**, 11799–11805 (2005).

11. X. Liu, X. Li, D. Kim, I. Ilev, and J. U. Kang, "Fiber-optic Fourier-domain common-path OCT," *Chin. Opt. Lett.* **6**(12), 899–901 (2008).
12. A. F. Fercher, W. Drexler, C. K. Hitzenberger, and T. Lasser, "Optical coherence tomography - principles and applications," *Rep. Prog. Phys.* **66**(2), 239–303 (2003).
13. B. E. Bouma, and G. J. Tearney, *Handbook of Optical Coherence Tomography*, (Marcel Dekker, New York, 2002).
14. Y. R. Chen, B. Sun, T. Han, Y. F. Kong, C. H. Xu, P. Zhou, X. F. Li, S. Y. Wang, Y. X. Zheng, and L. Y. Chen, "Densely folded spectral images of the CCD spectrometer working in the full 200-1000nm wavelength range with high resolution," *Opt. Express* **13**(25), 10049–10054 (2005), <http://www.opticsinfobase.org/oe/abstract.cfm?URI=oe-13-25-10049>.
15. M. Mujat, B. H. Park, B. Cense, T. C. Chen, and J. F. de Boer, "Autocalibration of spectral-domain optical coherence tomography spectrometers for in vivo quantitative retinal nerve fiber layer birefringence determination," *J. Biomed. Opt.* **12**(4), 041205 (2007).
16. C. Ding, P. Bu, X. Wang, and O. Sasaki, "A new spectral calibration method for Fourier domain optical coherence tomography," *Optik (Stuttg.)* **121**(11), 965–970 (2010).
17. E. Azimi, B. Liu, and M. E. Brezinski, "Real-time and high-performance calibration method for high-speed swept-source optical coherence tomography," *J. Biomed. Opt.* **15**(1), 016005 (2010).
18. J. Xi, L. Huo, J. Li, and X. Li, "Generic real-time uniform K-space sampling method for high-speed swept-Source optical coherence tomography," *Opt. Express* **18**(9), 9511–9517 (2010), <http://www.opticsinfobase.org/abstract.cfm?URI=oe-18-9-9511>.
19. N. V. Iftimia, D. X. Hammer, R. D. Ferguson, M. Mujat, D. Vu, and A. A. Ferrante, "Dual-beam Fourier domain optical Doppler tomography of zebrafish," *Opt. Express* **16**(18), 13624–13636 (2008), <http://www.opticsinfobase.org/abstract.cfm?URI=oe-16-18-13624>.
20. A. Uneri, M. Balicki, J. Handa, P. Gehlbach, R. Taylor, and I. Iordachita, "New Steady-Hand Eye Robot with Microforce Sensing for Vitreoretinal Surgery Research," *IEEE BioRob* (2010).
21. M. Wojtkowski, V. Srinivasan, T. Ko, J. Fujimoto, A. Kowalczyk, and J. Duker, "Ultrahigh-resolution, high-speed, Fourier domain optical coherence tomography and methods for dispersion compensation," *Opt. Express* **12**(11), 2404–2422 (2004), <http://www.opticsinfobase.org/oe/abstract.cfm?URI=oe-12-11-2404>.
22. Y. Yasuno, Y. Hong, S. Makita, M. Yamanari, M. Akiba, M. Miura, and T. Yatagai, "In vivo high-contrast imaging of deep posterior eye by 1-um swept source optical coherence tomography and scattering optical coherence angiography," *Opt. Express* **15**(10), 6121–6139 (2007), <http://www.opticsinfobase.org/oe/abstract.cfm?URI=oe-15-10-6121>.
23. X. Liu, E. Meisne, J. Han, K. Zhang, P. Gehlbach, and R. Taylor, "Internal limiting membrane layer visualization and vitreoretinal surgery guidance using OCT integrated microsurgical tool," *Proc. SPIE* **7550**, 755003 (2010).
24. J. U. Kang, J. Han, X. Liu, K. Zhang, C. Song, and P. Gehlbach, "Endoscopic Functional Fourier Domain Common Path Optical Coherence Tomography for Microsurgery," *IEEE J. Sel. Top. Quantum Electron.* **16**(4), 781–792 (2010), doi:10.1109/JSTQE.2009.2031597.
25. Z. Xu, L. Carrion, and R. Maciejko, "A zero-crossing detection method applied to Doppler OCT," *Opt. Express* **16**(7), 4394–4412 (2008), <http://www.opticsinfobase.org/abstract.cfm?URI=oe-16-7-4394>.
26. B. Cense, N. Nassif, T. Chen, M. Pierce, S. H. Yun, B. Park, B. Bouma, G. Tearney, and J. de Boer, "Ultrahigh-resolution high-speed retinal imaging using spectral-domain optical coherence tomography," *Opt. Express* **12**(11), 2435–2447 (2004), <http://www.opticsinfobase.org/oe/abstract.cfm?URI=oe-12-11-2435>.

## 1. Introduction

Integrating optical coherence tomography (OCT) in handheld or robot-assisted surgical tools for microsurgery can potentially minimize damage to tissue and improve surgical outcomes [1–5]. Fourier Domain OCT (FD OCT), which offers significantly improved sensitivity and imaging speed compared to time-domain OCT (TD-OCT) [6–11], has been incorporated with robotic surgical tools for vitreoretinal surgery applications. For example, such systems can use real-time, tool-to-tissue range data derived from OCT images to actively enforce safety barriers, compensate for patient motion, or guide the surgeon to perform a pre-planned maneuver [2,3]. In such applications, it is critical for OCT to have high axial imaging resolution and precise depth ranging functionality. Further, safety, reliability, and ease of use are important factors in a demanding application like microsurgery, where imaging devices are exposed to extreme handling conditions, require frequent safety checks, and redundant monitoring during operation.

FD OCT has two subcategories: 1) spectral domain OCT and 2) swept-source OCT [12,13]. In this paper, "FD OCT" specifically refers to spectral domain OCT, which uses a spectrometer to detect spectral interferograms. To achieve high axial resolution and ranging accuracy, FD OCT requires not only a broadband light source and a well-designed

spectrometer, but also an accurate spectral calibration to correctly reconstruct the sample's depth profile (A-scan). To obtain an A-scan from the spectral interferogram captured by the spectrometer, an inverse Fourier transformation is applied to the interference spectral data that is evenly spaced in wavenumber space (k-space) [14–18]. However, in FD OCT, the spectra are detected by CCD or CMOS arrays, which usually do not guarantee an uniform sampling in k-space. Converting the data from pixel space to k-space depends on knowing the wavenumber at each pixel of the array detector, which is usually determined through a calibration process. Poor or imprecise calibration results in a point spread function (PSF) that has a depth-dependent broadening, analogous to pulse broadening induced by group velocity dispersion. Besides significantly degrading system performance in terms of the resolution and sensitivity, an inaccurate calibration also leads to erroneous depth ranging.

Calibration of a spectrometer in FD OCT can be achieved either by measuring the spectrum of an external calibrating light source with known spectral features [14] or by comparing spectral interferograms measured with the OCT spectrometer to measurements made by a well-calibrated commercial optical spectrum analyzer (OSA) [16]. However, these conventional calibration methods are time-consuming and require separate measurements and extra equipment. These factors make conventional calibrations inconvenient in a clinical setting. Moreover, the characteristics of a spectrometer will naturally change over time, due both to environmental effects such as temperature and vibration and to poor handling practices [15]. Therefore, monitoring and recalibration of the spectrometer may be necessary for each FD OCT measurement session. Furthermore, when using OCT in imaging and servoing for image-guided, robot-assisted surgery, the refractive index of the medium might be unknown and thus will impose a challenge in accurately determining the distance between the probe and sample surfaces. Since OCT measures optical path length, which is the product of physical distance and medium's refractive index, a wrong estimation of this physical distance can cause inaccuracies in imaging, targeting errors, and robot control instabilities. All are unacceptable for high-risk microsurgical applications. A simple and automatic OCT calibration protocol that addresses these issues is required.

M. Mujat *et al* reported an automatic spectrometer calibration, based on generating a perfect sinusoidal spectral modulation in k-space by inserting a thin glass slide into the optical path [15]. Algorithm used in [15] requires that the spectrum has a perfect sinusoidal modulation; otherwise, it is impossible to obtain the phase for calibration. Moreover, M. Mujat *et al*'s calibration does not produce the values for wavenumber limits; therefore, the physical pixel spacing of the OCT A-scan is still unclear after calibration. The specular reflection of the inserted glass slide may occupy a large portion of the detector's dynamic range, thus may reduce the dynamic range usable for sample and reference signal; on the other hand, the reduction of power from the broadband source may reduce system's sensitivity. In Iftimia *et al*'s spectral calibration, they circumvented the abovementioned problems by inserting the glass slide into the reference arm with power attenuation [19].

In this paper, we present a new automatic spectral calibration method for FD OCT. The method was tested using a common path FD OCT integrated with a robotic microsurgical assistant system called the EyeRobot [2,20]. However, our calibration is essentially a generic, automatic spectral calibration (ASC) method that can be implemented in any spectrometer-based FD OCT system coupled with a precise axial positioning actuator, which is often used in OCT scanners.

The proposed ASC method does not require the use of an external light source or a commercial OSA. Moreover, we use a zero-crossing detection technique which offers an accurate estimation of wavenumber's functional dependency on pixel index, even when the spectrum does not have a perfect sinusoidal modulation. In our algorithm, we further correct the spectral mapping obtained from zero-crossing detection using an iterative optimization [21,22]. As a result, spectral interferograms used in our ASC method can be directly derived from an arbitrary sample—even with complex internal structures like the ones found in

biological samples. Therefore, a specimen itself can be used to generate data to calibrate the OCT system during scanning. To extract the pixel spacing of OCT A-scan, we adjust the axial distance between the reference plane and the sample surface by the commanded motion of our robot which is holding the probe of our FD OCT. The pixel spacing is obtained through a least square linear regression based on the known robot motion and the depth ranging derived from the OCT signal. Furthermore, in the case where the sample might be moving, we modulate the motion of the robot sinusoidally to encode its position relative to the moving sample. The motion is then extracted from the A-scans to calculate the physical pixel spacing.

To test the performance of the proposed calibration method, we measured the system's axial PSF at different imaging depths; the results showed an axial resolution better than  $4\mu\text{m}$  over the entire imaging depth of interest. After calibrating the A-scan pixel spacing, we achieved high ranging accuracy and the ranging error is within system's tolerance. We finally performed OCT scans to a multilayered phantom as well as to human subject in vivo. 2D images revealing sample structure were obtained through our automatic spectral calibration.

## 2. CP FD OCT & robotic scanning system

In this study, a Common Path FD OCT (CP FD OCT) is integrated with the EyeRobot. We adopt CP FD OCT because it is a simple, compact system; the small probe size facilitates the integration of OCT with various robotic systems [2,23]. The reference light in CP OCT is derived from the distal end of the probe, which is also the tool tip; therefore, the sample-reference distance measured by CP FD OCT is virtually the tool-to-tissue distance, which is of great importance in robotic surgical servoing. Moreover, the shared reference and sample arms enable us to use a single-mode fiber probe with arbitrary length without concerns of chromatic dispersion mismatch [9,10,24].

As shown in Fig. 1, the CP FD OCT system consists of a single-mode fiber probe, a fiber-optic coupler which launches the source output to a sample as well as collects back reflected/scattered light. The tip of the single-mode fiber probe is cleaved at right angle to provide the reference light. We used a broadband source in the CP FD OCT system to achieve high axial resolution. We multiplexed three superluminescent emission diodes (SLED) from Exolas Inc. to form a broadband source that has a central wavelength of 800nm and a full width half maximum (FWHM) of 106nm. We built a custom spectrometer to detect the spectral interferograms for OCT image formation. It is built using a collimator, 1200-line pair-per-mm diffraction grating, an achromatic lens with 100mm focal length and a 2048 pixel CCD with  $14\mu\text{m}$  pixel size (e2v AVIIVA SM2 CL 2014, 28 kHz line scan rate). The camera integration time is set to  $1\mu\text{s}$  to avoid any motion artifacts.

The robot used in this study is a cooperatively controlled robotic assistant where the surgeon and robot both hold the surgical tool; the robot senses forces exerted by the surgeon on the tool handle and moves to comply with very high precision, inherently filtering out physiological hand tremor [20]. Furthermore, the robot controller can quickly switch between and/or combine the following modes: user guidance; sensor-based guidance; or predefined autonomous motion profiles. For the purpose of this study, we used only Cartesian positioning subsystem of the EyeRobot, consisting of three orthogonally mounted linear stages with positioning resolution of  $1\mu\text{m}$  and measured precision of about  $\pm 1\mu\text{m}$  over the range of motion required for this experiment ( $<4\text{mm}$ ). The single-mode fiber probe of CP FD OCT is attached to the tool holder of the EyeRobot, which scans the probe to obtain B mode or C mode OCT images, or actively servos surgical tasks [2]. The test samples are mounted on a separate actuated micrometer stage placed beneath the probe. The robot is guided directly by the operator to position the OCT probe above the desired scanning area of the sample.

The robot is interfaced to a PC workstation through a commercial motion controller (Galil DMC 1886), with software level servo loop operating at 500Hz. A 6 degree of freedom (DOF) force-torque sensor (ATI Nano43) is mounted on the robot near the OCT probe as a user interface for cooperative, "hands-on" control. The OCT application is implemented on a

separate PC and communicates with the robot PC via direct Ethernet link, with a fraction of ms latency.

It is worth mentioning that CP FD OCT with bare-fiber probe suffers from significant signal decay with increased imaging depth, especially above 500 $\mu\text{m}$ . This is because without a focusing lens at the sample arm, the light beam exiting the fiber tip diverges significantly as it propagates farther. However, this is not an issue for our application where the tool for surgical intervention is placed extremely close to the interrogated tissue.

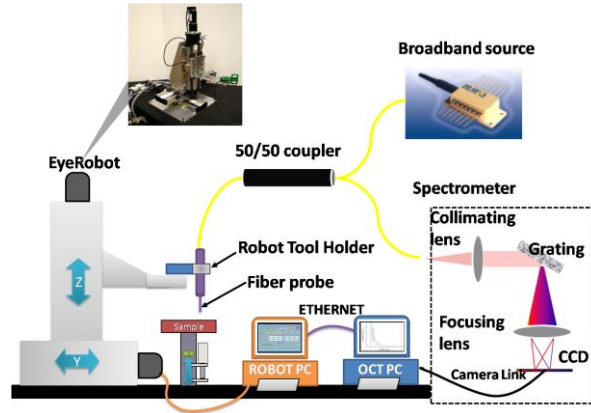


Fig. 1. Schematic of CP FD OCT and robot system.

### 3. Methods

As a result of interference between the reference and sample light, a spectral interferogram can be obtained.  $S_n$ , the spectral intensity of the interference term detected by the  $n^{\text{th}}$  pixel of the CCD, can be expressed as:

$$S_n = \alpha S_0(k_n) \sum_m [R_m \cos(2k_n l_m)] \quad (1)$$

In Eq. (1),  $k_n$  is the wavenumber corresponding to the  $n^{\text{th}}$  element of the CCD array;  $S_0$  indicates source spectrum;  $l_m$  indicates the path length difference between reference and sample plane;  $R_m$  indicates the sample reflectivity;  $\alpha$  is system's responsivity.

When inverse fast Fourier transformation (*IFFT*) is performed on the spectral interferogram to reconstruct sample's depth profile, it requires that the spectral interferogram is evenly sampled in k-space. However,  $k_n$  in Eq. (1), usually does not linearly depend on  $n$ . Therefore  $S_n$  has to be converted to k-space before *IFFT* [7,8,12], which requires us to know the wavenumber corresponding to each pixel. Assuming wavenumber  $k$  has a 4th order polynomial dependency on  $n$ , as shown in Eq. (2), our first task in ASC is to determine coefficients of the polynomial.

$$k_n = a_4 n^4 + a_3 n^3 + a_2 n^2 + a_1 n + a_0 \quad (2)$$

M. Mujat *et al.* obtained the functional dependency of wavenumber on the pixel indices by retrieving the phase from spectral interferogram [15]. However, when an arbitrary sample with complex internal structures is imaged, simply extracting the phase of interferogram,  $p(n)$ , does not lead us to know  $k_n$ . Nevertheless, the spectral mapping may still be achieved by using a zero-crossing detection technique, which has been used in processing Doppler OCT signals [25]. The zero-crossing detection for spectrum is based on the simple and important fact that zero-crossing points in a spectral interferogram are almost evenly spaced in k-space with a spectral interval  $\delta k$ . Although signals come from different depths and result in different frequency components in the spectral interferogram, the surface reflection of the sample

generates a large spectral modulation due to a refractive index discontinuity, and essentially determines the “fundamental frequency” of interference fringe, which is  $1/\delta k$ .

To reduce the probability of error in zero-crossing detection, we first apply a bandpass filter centering at the fundamental frequency of the spectral interference fringes, which simultaneously removes the autocorrelation term or DC component in the spectrum. Afterwards, we calculate the zero-crossing points by finding all pairs of adjacent pixels that have signal values with opposite signs. The  $m^{\text{th}}$  zero-crossing point  $n_m$  is obtained using a simple linear triangulation formula as shown in Eq. (3), in which  $S_{n_1}$  and  $S_{n_1+1}$  are spectral signal at the  $n_1^{\text{th}}$  and  $(n_1 + 1)^{\text{th}}$  pixels and have different signs [25].

$$n_m = \frac{n_1 S_{n_1+1} - (n_1 + 1) S_{n_1}}{S_{n_1+1} - S_{n_1}} \quad (3)$$

The wavenumbers corresponding to the zero-crossing points are known to be an integral multiple of  $\delta k$  plus a constant offset, as shown in Eq. (4):

$$k(n_m) = m\delta k + k_0 \quad (4)$$

Translating and scaling  $k(n_m)$ , we have:

$$\tilde{k}(n_m) = \frac{k(n_m) - k_0}{\delta k} \quad (5)$$

Given that  $k(n)$  is a polynomial and so is  $\tilde{k}(n_m)$ , the polynomial coefficients that define  $\tilde{k}(n_m)$  can be found through the least-squares polynomial fitting, using the known function value of  $\tilde{k}(n_m)$  which is integer  $m$ , and the corresponding variable  $n_m$ . Therefore, with the obtained polynomial, the wavenumber at each pixel is known up to a scaling factor  $\delta k$  and an offset  $k_0$ . To convert the spectral data into wavenumber space, we can generate an array  $\hat{k}_n$  which has the same extremes as  $\tilde{k}(n)$  and contains elements with evenly spaced values. Afterwards, we use a spline interpolation to obtain spectral data corresponding to wavenumbers in  $\hat{k}_n$  using the detected signal corresponding to  $\tilde{k}(n)$ . Finally, performing *IFFT* on the spectral interferogram generated by interpolation will lead to OCT A-scan.

Due to inevitable errors in zero-crossing detection, the polynomial coefficients obtained might be imprecise; therefore, it is necessary to further refine the polynomial coefficients. Since a more accurate spectral calibration allows us to reconstruct an OCT image with better energy concentration or image sharpness [24,25], we may refine the polynomial coefficients by an iterative algorithm, which effectively maximizes the sharpness of OCT A-scans. A similar algorithm has been used in numerical dispersion compensation by correcting the nonlinear phase in ultrahigh resolution OCT. To measure the image sharpness, we use a quantity  $\mathbf{M}$  (also defined in [24]), which equals one divided by the total number of points in the A-scan with intensity larger than a predetermined threshold. Starting from an initial estimation of  $a_4, a_3, a_2, a_1$  and  $a_0$  based on the result of zero-crossing detection, we iteratively correct polynomial coefficients to maximize  $\mathbf{M}$  through an unconstrained nonlinear optimization that searches the  $(a_1, a_2, a_3, a_4)$  space. Although chromatic dispersion mismatch may also reduce energy concentration in OCT image, image degradation induced by dispersion mismatch is negligible compared to the inaccuracy in calibration when CP FD OCT is used, as in our case.

The zero-crossing detection is a critical first step in our calibration, because it gives an accurate estimation of  $k(n)$  as the starting point for the iterative corrections. The objective function of the optimization problem  $\mathbf{M}$  may have multiple local optimums in the space searched. Starting from a point close to the global optimum, i.e., using a more accurate estimation of  $k(n)$ , as the initial condition, the iteration can converge to the solution at a faster

speed with higher reliability. Otherwise, it is likely that the iteration converges to a local optimum which does not correspond to the correct solution. Especially, a system with a large  $k$  nonlinearity or dispersion mismatch would likely encounter this problem.

To show that that zero-crossing detection can offer a more accurate estimation of  $k(n)$  than from phase directly extracted from the real valued spectrum,  $p(n)$ , we performed the following numerical study. Assuming the spectrometer covers a spectral range from 700 to 900nm and the CCD array samples the spectrum linearly in wavelength space, we calculated  $k(n)$  as shown in Fig. 2(a), which is used as a baseline to compare with the spectral mapping result we inversely extracted from our simulating data. FD OCT signal was generated assuming that the sample has an unit reflectivity at 50 $\mu$ m away from the reference, which is the sample surface; and we used uniformly distributed random numbers within [0 R] (R is a positive real value) to simulate the reflectivity from 50 $\mu$ m to 500 $\mu$ m in depth. Taking signal attenuation into a consideration, we applied an exponential function with a decay constant of 200 $\mu$ m to the depth profile. Modeling the source spectrum as a Gaussian function with a FWHM of 100nm, we generated interferometric spectrum based on the simulated reflectivity profile according to Eq. (1). An example of the interferometric spectrum is shown in Fig. 2(b) (R = 0.2), corresponding to the sample profile shown in Fig. 2(c). Using the simulated spectral data, we can obtain  $\tilde{k}(n)$  by zero crossing detection; while we can also obtain the phase  $p(n)$  from the real valued spectrum by Hilbert transforming spectrum shown in Fig. 2(b).  $k(n)$ ,  $\tilde{k}(n)$ ,  $p(n)$ , as well as the 4th order polynomial fit of  $p(n)$  are all rescaled to [0, 1]. We show the differences between  $k(n)$  and  $\tilde{k}(n)$ ,  $k(n)$  and  $p(n)$ ,  $k(n)$  and the 4th order polynomial fit of  $p(n)$  in Fig. 2(d)–2(f), with R equals 0.1, 0.2, and 0.3 respectively. It is clear in Fig. 2 that zero-crossing detection offers a better estimation of  $k(n)$  than phase directly extracted from the interferometric spectrum.

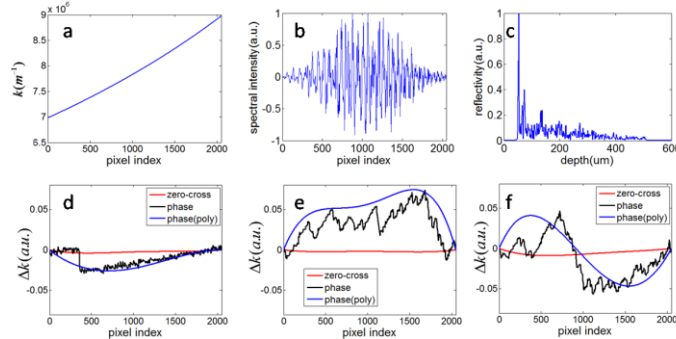


Fig. 2. (a) Wavenumber versus pixel index; (b) simulated interferometric fringes in pixel space; (c) A-scan corresponding to spectrum in Fig. 2(b); differences between  $k(n)$  and  $\tilde{k}(n)$ ,  $k(n)$  and  $p(n)$ ,  $k(n)$  and the 4th order polynomial fits of  $p(n)$  for data generated with R equals 0.1(d), 0.2(e), and 0.3(f).

The second part of our ASC method is to obtain the physical spacing between two adjacent pixels in OCT A-scan,  $\Delta z$ , which can be calculated using Eq. (6) [8]:

$$\Delta z = \frac{\pi}{\eta \Delta k} \quad (6)$$

Equation (6) calculates  $\Delta z$  using  $\eta$ , medium's refractive index, and  $\Delta k$ , the spectral range covered by the spectrometer, both of which might be unknown in practice. As a result, instead of calculating  $\Delta z$  with Eq. (6), we obtain  $\Delta z$  by comparing the commanded EyeRobot motion and ranging data derived from the OCT when we use the EyeRobot to precisely adjust the distance between the sample and reference plane.

With the single-mode fiber probe attached to the tool holder of the EyeRobot and a sample fixed to a stage, the distance between the reference plane and sample surface changes as the EyeRobot moves axially with respect to the sample surface. We recorded interferograms corresponding to different imaging depths. Converting spectral data to k-space based on obtained polynomial coefficients and performing *IFFT*, we obtain A-scans that have peaks indicating the interface between air and sample's surface. The indices of peak pixels are obtained by a peak searching algorithm and are denoted by  $i_1$ ,  $i_2$  and  $i_{3,\dots}$ , corresponding to different z-positions of the robot  $Z_1$ ,  $Z_2$  and  $Z_3$  [3]. Using a vector  $\mathbf{i}$  to indicate  $i_1$ ,  $i_2$  and  $i_{3,\dots}$ , a vector  $\mathbf{Z}$  to indicate  $Z_1$ ,  $Z_2$  and  $Z_{3,\dots}$ , we have:

$$\mathbf{Z} = \mathbf{i}\Delta z + z_0 \quad (7)$$

The pixel spacing  $\Delta z$  can thus be obtained by regression using a least square fit of the linear model shown above.

However, the ranging data derived from OCT, i.e., the pixel index of the A-scan peak, may be corrupted by the unknown motion of the sample, such would be the case when trying to obtain calibration data from a live specimen. It is therefore problematic to obtain the pixel spacing  $\Delta z$  based on Eq. (7). However, a simple sinusoidal modulation of the EyeRobot Z position would allow us to easily differentiate the deterministic displacement of robot,  $\mathbf{Z}$ , and random sample displacement,  $\mathbf{Z}_s$ . Taking into account the robot's known motion and the sample's random motion, we may rewrite Eq. (7) as:

$$Z_0 \sin(\omega t) + Z_s(t) = \mathbf{i}(t)\Delta z + z_0 \quad (8)$$

Due to the sinusoidal modulation of the EyeRobot  $\mathbf{Z}$  position, performing Fourier transform on  $i(t)$  leads to a high peak corresponding to the modulation frequency  $\omega$ . It is unlikely that the sample's motion has the same frequency component; therefore, filtering the signal corresponding to the modulation frequency out and denoting the result as  $\hat{i}(t)$ , which is related to the commanded motion of the probe, we have:

$$Z_0 \sin(\omega t) = \hat{i}\Delta z + \hat{z}_0 \quad (9)$$

Based on the linear model shown in Eq. (9), we can obtain the pixel spacing  $\Delta z$  by least square regression, even with unknown sample motion.

#### 4. Experiments and results

We used a multilayered phantom sample that consisted of 6 layers of cellophane tape to generate data for our calibration. We changed the robot position vertically with respect to the surface of the phantom at  $2\mu\text{m}$  increments and recorded 250 interferograms at resulting imaging depths. In principle, any of the interferograms can be used for ASC. However, an interferogram that has a larger fringe period will result in reduced error in zero-crossing detection; an interferogram that has a smaller fringe period will generate more zero-crossing points for the polynomial curve fitting. The spectrum used for calibration has to balance this tradeoff. In obtaining plots in Fig. 3, we used an interferogram obtained when sample surface was about  $120\mu\text{m}$  away from the reference plane for the calibration. Figure 3(a) shows a section of the spectrum used for calibration, in which the red and black curves are the original spectrum and the spectrum after bandpass filtering; the blue circles indicate zero-crossing points.

Figure 3(b) shows the initial estimation of  $\tilde{k}(n)$ , obtained by polynomial curve fitting the zero-crossing points. We offset the  $\tilde{k}(n)$  values and applied a scaling factor, so that  $\tilde{k}(n)$  ranges from 0 to 2047. Using the initial estimation of  $\tilde{k}(n)$ , we converted all the 250 spectra to k-space and performed *IFFT* to obtain A-scans. We iteratively corrected the coefficients  $a_1$ ,  $a_2$ ,  $a_3$ , and  $a_4$  to maximize the mean value of the sharpness merit  $\mathbf{M}$  of all the A-scans. In

Fig. 3(c) we plotted the difference between the initial estimation of polynomial function and polynomial function that maximizes A-scan sharpness. Based on  $\tilde{k}(n)$  shown in Fig. 3(b) and the adjustment shown in Fig. 3(c), we can convert the spectrum from pixel space to k-space, as shown in Fig. 3(d) (blue, the spectrum in pixel space; red, the spectrum that has been converted to k-space). Performing *IFFT* on the k-space spectral interferogram shown as the red curve in Fig. 3(d), we are able to obtain the A-scan shown in Fig. 3(e), which indicates that the sample used to generate calibrating data has complex internal structures.

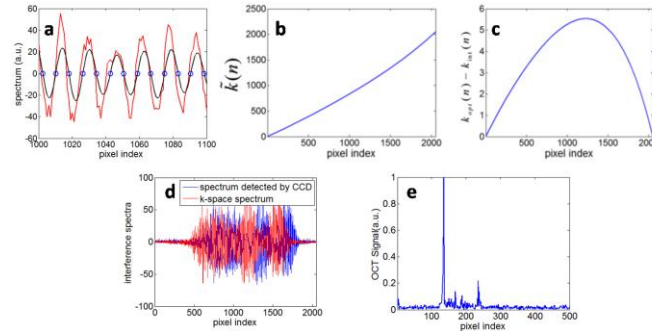


Fig. 3. (a) Interferometric fringes detected at the center part of CCD (red, original spectrum; black, spectrum after bandpass filtering; blue circles, zero-crossing points); (b) initial wavenumber mapping using zero-crossing detection; (c) difference between the initial estimation of wavenumber mapping and the wavenumber mapping that maximizes A-scan sharpness; (d) interferometric fringes obtained from multilayered phantom, in pixel space (blue) and k-space (red). (e) A-scan corresponding to the spectrum in Fig. 3(d).

Based on the polynomial  $\tilde{k}(n)$  obtained after the iterative algorithm, we convert all the 250 spectra to k-space and obtain A-scans that have different peak indices, shown as M-scan in Fig. 4(a). Figure 4(b) shows the distance between reference plane and sample surface derived from the OCT signal (upper) and the command that drives the robot motion (lower). Assuming the sample is static, we obtain the pixel spacing  $\Delta z$  in A-scan to be  $1.6\mu\text{m}/\text{pixel}$  by solving the linear model shown in Eq. (5) by least square regression. The R-square statistic of the regression is larger than 0.99, indicating the result is highly reliable. To test the ranging accuracy, we conducted another experiment. We imaged a mirror at different imaging depths and detected the index of signal peak of A-scan and calculated the robot z-position  $\tilde{Z}$  with Eq. (5). Applying offsets to  $\tilde{Z}$  and the commanded robot displacement  $Z$  so that they both start from 0, we compared  $\tilde{Z}$  with  $Z$ . The difference between  $\tilde{Z}$  and  $Z$  is shown in Fig. 4(c), which has a mean of  $0.14\mu\text{m}$  and a standard deviation of  $0.61\mu\text{m}$ . The small mean value indicates a high ranging accuracy over the imaging depth of interest. The  $0.61\mu\text{m}$  standard deviation falls within the system tolerance and the ranging error mainly come from the positioning error of the robot and the finite OCT pixel spacing.

In order to calibrate the pixel spacing with a nonstatic sample, we modulated the robot's Z position with 1Hz,  $400\mu\text{m}$  peak-to-peak sinusoidal wave. The sample, a multilayered cellophane-tape phantom, was driven by an actuator by a 10Hz sinusoidal wave to move in-line with the robot's Z axis. Using one of the interferograms to generate calibrating polynomial, we obtained an M-scan as shown in Fig. 4(d). For each A-scan in Fig. 4(d), we detect the peak index. The peak indices in the A-scans, corresponding to the surface of our phantom, are plotted in Fig. 4(e). The lower plot in Fig. 4(e) shows the result of frequency analysis of the signal peak position. Two frequency peaks appear at 1Hz and 10Hz, corresponding to the motion of the robot and the sample, respectively. Using a bandpass filter, we were able to separate the known robot motion at 1Hz from the sample motion. Figure 4(f) shows the robot position in pixel derived from OCT signal after bandpass filtering (upper) and

commanded robot position in mm (lower). Using results shown in Fig. 4(f) and performing regression as shown in Eq. (7), we calculated the pixel spacing to be  $1.6\mu\text{m}/\text{pixel}$ , which is identical to our previous result. Figure 4(g) shows the difference between robot z-position (distance to sample surface) measured with the OCT and commanded position.

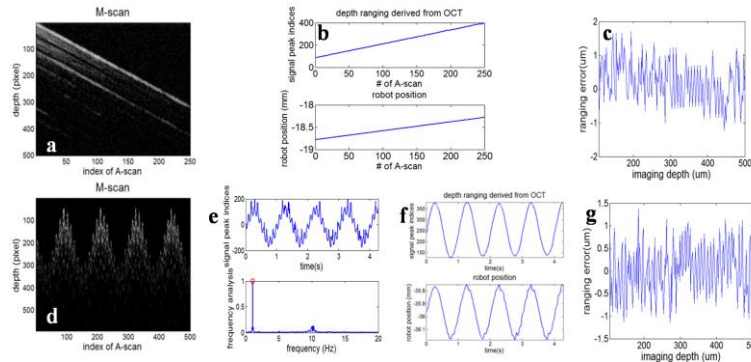


Fig. 4. (a) M-scan obtained when scanning the OCT probe axially above a multilayered phantom; (b) robot motion derived from OCT signal in the unit of pixel (upper); commanded robot motion in the unit of mm(lower); (c) ranging error based on regression using Fig. 4(b); (d) M-scan obtained when the OCT probe was modulated sinusoidally and the sample was nonstatic; (e) peak indices of OCT signal (upper) and its frequency analysis result (lower); (f) robot motion derived from OCT signal in the unit of pixel (upper); commanded robot motion in mm (lower); (g) ranging error based on regression of Fig. 4(f).

To evaluate the performance of the ASC method, we measured the axial PSF of our system by imaging a mirror at different depths. Figure 5(a), 5(b), and 5(c) show PSFs obtained without converting the spectral data to k-space, PSFs obtained from k-space spectral data using the initial estimation of the 4th order polynomial, and PSFs obtained from k-space spectral data using 4th order polynomial that maximizes the image sharpness. Figure 5(a) shows the extremely broadened PSFs. PSFs in Fig. 5(b) and 5(c) are much narrower compared to the ones in Fig. 5(a). While PSFs in Fig. 5(b) show slight broadening as the imaging depth increases, PSFs in Fig. 5(c) stay almost constant over the entire imaging depth. The difference can be more clearly seen in Fig. 5(d), which shows the axial resolution defined as the FWHM of the PSF at various imaging depths. When the optical path length difference between the reference and sample is small, both calibrations lead to about  $3.2\mu\text{m}$  resolution. With a larger distance between the reference and sample, the calibration based on the initial estimation of polynomial leads to a poorer resolution.

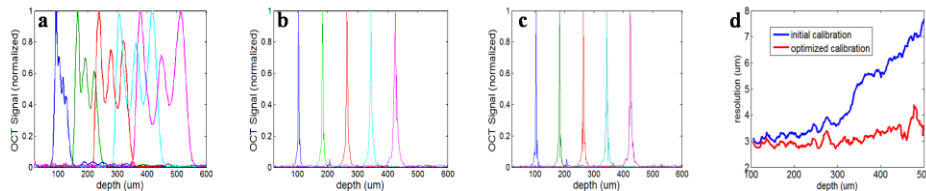


Fig. 5. (a) PSFs obtained without calibration; (b) PSFs obtained with calibration based on the initial estimation of the 4th order polynomial; (c) PSFs obtained with calibration based on the 4th order polynomial that maximizes the image sharpness; (d) FWHM resolution at different depths based on initial estimation of polynomial (blue) and the polynomial that maximizes the signal sharpness (red).

To demonstrate that calibrating data generated from a multilayered phantom can lead to comparable performance as calibrating data generated from an ideal reflector with a perfect sinusoidal modulation, we used our CP FD OCT to image a mirror and calibrated our spectrometer by extracting the phase of the interferogram using a similar method as one

proposed by M. Mujat *et al* [15]. The obtained  $k(n)$  is rescaled to [0 1] and shown in Fig. 6(a), which will be used as a ground truth to compare with result of our ASC method obtained from a multilayered sample. We evaluated the performance of calibration using axial resolution defined as FWHM of the PSF. Based on the calibrating polynomials obtained, we measured the axial resolution  $\delta z_{ASC}$  and  $\delta z_{groundtruth}$  at different imaging depths, where see Fig. 6(b). Although the interferograms captured from a multilayered phantom and mirror are significantly different, Fig. 6(b) shows that the performances of ASC using a multilayered phantom and the ground truth calibration using a mirror are similar. We calculated the difference between  $\delta z_{ASC}$  and  $\delta z_{groundtruth}$ ; the difference between them turned out to have a mean value of  $0.1129\mu\text{m}$ , indicating that our ASC using a sample with complex internal structure has satisfactory performance compared to conventional spectral calibration methods.

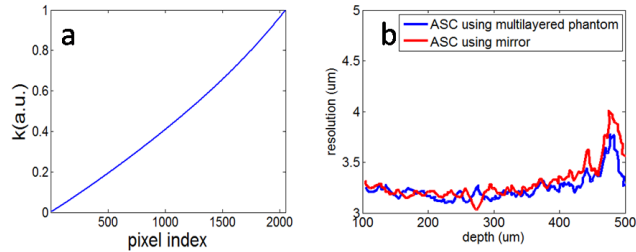


Fig. 6. (a) ground truth spectral mapping obtained from a mirror: wavenumber versus pixel index in our spectrometer; (b) FWHM resolution at different depths using interferograms from a multilayered phantom by ASC (blue) and from a mirror by extracting the phase (red).

We scanned the fiber probe laterally over the multilayered phantom and obtained a B-mode OCT image based on the result of our ASC. The result is shown in Fig. 7(a) and the scale bar indicates  $100\mu\text{m}$ . In Fig. 7(a), tape layers are clearly visible. As a comparison, Fig. 7(b) shows the OCT image obtained by directly performing *IFFT* on the spectral data detected by CCD, in which the layer structure is hardly discernable.

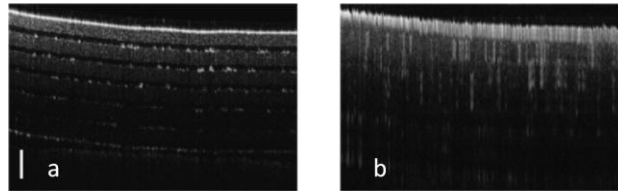


Fig. 7. Image of multilayer phantom obtained with (a) and without (b) ASC.

To show that our automatic calibration algorithm works for human tissue, *in vivo*, we scanned the forearm of a healthy human volunteer. We chose one interferometric spectrum obtained from human subject for the automatic spectral calibration. Again, we use the ground truth calibration shown in Fig. 6(a) for comparison. The particular spectrum is subsequently converted to k-space according to the “ground truth” calibration result, and according to the result based on our ASC algorithm which uses the same spectrum to generate spectral mapping. The obtained A-scans in linear scale are shown in Fig. 8(a) as red and blue curves. It shows that the human tissue surface generates a sufficiently strong signal peak for ASC algorithm; moreover, A-scans overlap well. We processed all the obtained spectra and show the resultant 2D images (logarithmic scale) in Fig. 8(b) and 8(c), which are based on ground truth calibration and the ASC method using sample interferogram, respectively. In both images, stratum corneum (SC), epidermis (EP) and dermis (DE) are visible. We obtained identical images using both calibrations, which verifies the effectiveness of our algorithm for *in vivo* data.

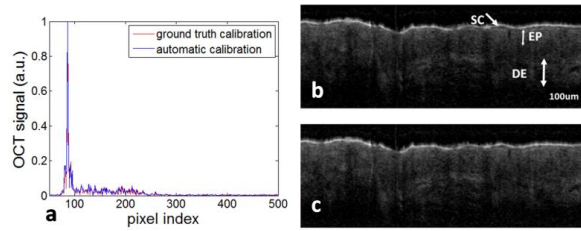


Fig. 8. (a) A-scans based on ground truth calibration and ASC; (b) OCT image (logarithmic scale) of human forearm skin, based on ground truth calibration(SC: stratum corneum; epidermis: EP; dermis: DE); (c) OCT image (logarithmic scale) of human forearm skin, based on our automatic calibration using sample interferogram.

## 5. Discussion and conclusions

While OCT systems are typically calibrated in a lab setting, our method can be used “on-the-fly” which allows monitoring of OCT system performance during scanning operation or between scans. This is possible because the spectral data for our ASC method is a conventionally scanned image, i.e., spectral interferogram captured from a sample with complex internal structures. This is a very compelling feature for safety reasons as well as convenience - especially for portable systems that might be used in surgical settings or any mission critical applications.

Furthermore, when using the OCT data for image-guided interventions or general metrology, pixel size calibration is necessary. We achieved the A-scan pixel size calibration by modulating the motion of the robot holding the probe to encode its position relative to the moving sample. This relative motion is extracted from the OCT data and compared with the commanded robot motion. A simple regression procedure is used to extract the A-scan pixel size. The motion profile can be any function that is significantly different from the assumed sample motion. For robustness, we can use multiple, superimposed periodic profiles, e.g.,  $10\text{hz} + 3\text{hz}$ . Our method assumes that the sample motion is not affected by the motion of the probe. This might not be true if the displaced fluid in front of the oscillating probe compresses or translates the sample tissue, especially if the probe has a profile with large surface area and is close to the sample surface. In the future we will look into determining the affects of this on our calibration method. We are also planning to investigate minimum sinusoidal motion amplitude required to produce satisfactory results. Although our application requires a sophisticated surgical robot, the proposed A-Scan pixel spacing calibration applies to systems integrated with an axial actuator that is readily available and can be performed with static or moving sample.

Due to the random nature of the scanning environment and complex sample structure, it is possible that a “bad” interferogram is captured that may not lead to a high quality calibration. This might be one drawback of our ASC method. However, during scanning multiple A-scans are often acquired and, thus, provide multiple samples from which we can choose the one leading to the optimized calibration result. Detecting such cases and selecting the best solutions will be investigated in the future.

It is worth mentioning that we demonstrate the ASC method in a common path OCT system, which is known to have neglectable systematic dispersion mismatch. If an OCT system suffers from both dispersion mismatch and non-equally k-space sampling, which is true for most OCT systems based on a Michelson interferometer [26], the result of our calibration is not merely a k-space calibration. However, it effectively compensates and corrects for any system induced phase chirp. Our results clearly show that it does so and the method would simultaneously calibrate the spectrometer and compensate for system dispersion mismatch in other types of spectral-domain OCT. Therefore, one can perform the whole procedure of spectral calibration we proposed to calibrate the any Michelson interferometer based SD OCT.

## **6. Conclusion**

In this work, we propose a novel automatic spectral calibration method. In our ASC method, the spectral mapping for an OCT spectrometer is performed during scanning of a sample. The obtained polynomial that relates wavenumber and pixel indices is used to reconstruct OCT images with maximized sharpness. Moreover, the A-scan pixel spacing can be extracted when the sample is static or dynamic. Using the probe-to-sample distance, derived from the OCT signal, and the commanded robot motion, we can obtain the pixel spacing using linear regression. The performance of ASC using spectral data from a complex sample is comparable to other calibration methods.

## **Acknowledgments**

The research reported in this paper was supported in part by National Institutes of Health (NIH) BRP grant 1 R01 EB 007969 and NIH R21 1R21NS063131-01A1, in part by fellowship support from the ARCS Foundation.